

# A Classical Chiral Spin-Liquid from Chiral Interactions on the Pyrochlore Lattice

Daniel Lozano-Gómez,<sup>1</sup> Yasir Iqbal,<sup>2</sup> and Matthias Vojta<sup>1</sup>

<sup>1</sup>*Institut für Theoretische Physik and Würzburg-Dresden Cluster of Excellence ct.qmat,  
Technische Universität Dresden, 01062 Dresden, Germany*

<sup>2</sup>*Department of Physics and Quantum Centre of Excellence for Diamond and Emergent Materials (QuCenDiEM),  
Indian Institute of Technology Madras, Chennai 600036, India*

(Dated: March 19, 2024)

Classical spin-liquids are paramagnetic phases which feature nontrivial patterns of spin correlations within their ground-state manifold whose degeneracy scales with system size. Often they harbor fractionalized excitations, and their low-energy fluctuations are described by emergent gauge theories. In this work, we discuss a model composed of chiral three-body spin interactions on the pyrochlore lattice that realizes a novel classical chiral spin-liquid. Employing both analytical and numerical techniques, we show that the ground-state manifold of this spin-liquid is given by a subset of the so-called color-ice states. We demonstrate that the ground states are captured by an effective gauge theory which possesses a divergence-free condition and an additional chiral term that constrains the total flux of the fields through a single tetrahedron. The divergence-free condition results in two-fold pinch points in the spin structure factor and the identification of bionic charges as the elementary excitations of the system. We discuss how the mobility of these elementary charges is restricted by the additional chiral term, which in turn suggests that these charges are fractons.

## I. INTRODUCTION

Spin-liquids are disordered yet highly correlated phases of matter whereby magnetic degrees of freedom evade symmetry-breaking long-range order down to lowest temperatures [1, 2]. It has been shown how such cooperative behavior can be succinctly described by emergent gauge symmetries [3, 4]. Frustrated Mott-insulating magnets have been established as the key platform to realize classical and quantum spin-liquids which can emerge as a consequence of competing interactions stemming from either the architecture of the underlying lattice or from strong spin-orbit coupling [5–12].

The pyrochlore lattice, composed of a network of corner-sharing tetrahedra with the magnetic ions located at the vertices, has proven to be an excellent arena for the realization of spin-liquid phases. In the classical realm, examples of such highly correlated phases include the well known spin-ice phase [4, 6, 13], the recent realizations of rank-2 spin-liquids [7–9, 14–16] as well as mixed rank-1–rank-2 spin-liquids [12]. All these liquid phases are realized in spin systems whose interactions are bilinear in the spin degrees of freedom, taking the form  $\mathbf{S}_i \mathcal{H}_{ij} \mathbf{S}_j$ , where  $\mathcal{H}_{ij}$  represents the bilinear coupling between the spins. Here, the  $\mathcal{H}_{ij}$  spin coupling matrix in the generic case encompasses both isotropic and anisotropic interactions between not only first but also farther neighbors. This includes the isotropic Heisenberg terms ( $\mathbf{S}_i \cdot \mathbf{S}_j$ ) [5, 17], as well as, anisotropic Ising ( $S_i^z S_j^z$ ) [16], Dzyaloshinskii-Moriya ( $\mathbf{D}_{ij} \cdot [\mathbf{S}_i \times \mathbf{S}_j]$ ) [18], and off-diagonal symmetric also known as pseudo-dipole ( $S_i^x S_j^y + x \leftrightarrow y$ ) [19], as well as their analogs for further-neighbor interaction terms [20–22].

In contrast, much less attention has been devoted to spin Hamiltonians with three-body or four-body spin interactions which might also offer the possibility of realizing spin-liquid phases. One example of such a higher-

body interaction is the isotropic biquadratic interaction  $(\mathbf{S}_i \cdot \mathbf{S}_j)^2$  [23, 24]. A recent work studied the physics resulting from the biquadratic coupling on the pyrochlore lattice with an additional Heisenberg term [23]. However, such a model features an order-by-disorder selection of a magnetically ordered state at low temperatures.

In the present paper, we consider the so-called scalar spin chiral term, a magnetic three-body interaction which arises in a  $t/U$  expansion of the Hubbard model at half-filling in the presence of a magnetic field [25]. This leads to the following spin-rotation invariant Hamiltonian which breaks time-reversal and parity symmetries [26, 27]

$$\mathcal{H}_\chi = -J_\chi \sum_{i,j,k \in \Delta} \chi_{ijk}, \quad (1)$$

where  $\chi_{ijk} = \mathbf{S}_i \cdot (\mathbf{S}_j \times \mathbf{S}_k)$ , with  $i, j, k$  being the corners of triangular faces in up and down tetrahedra. We have chosen the chirality such that, for an up tetrahedron, one term is  $\mathbf{S}_0 \cdot (\mathbf{S}_1 \times \mathbf{S}_2)$ , where  $\mathbf{S}_0$  is located at [000],  $\mathbf{S}_1$  at  $\frac{1}{4}[110]$ , and  $\mathbf{S}_2$  at  $\frac{1}{4}[101]$ , see Fig. 1. Schematically, the chirality of every triangular face of a single tetrahedron is associated with a chiral vector pointing *outwards* of its corresponding tetrahedron, such that we have a uniform chiral model.

The above Hamiltonian has previously been investigated on the kagome lattice, where both classical and quantum order-by-disorder mechanisms drive the system into a long-range ordered state where the spins in every triangle are constrained to point along one of the three *global* Cartesian axis [28]. Here, we shall study the classical limit ( $S \rightarrow \infty$ ) of the Hamiltonian in Eq. (1) on the pyrochlore lattice. We demonstrate that the system realizes a spin-liquid phase down to the lowest simulated temperatures. The ground-state manifold is characterized by the spins in every single tetrahedron pointing along four distinct directions, with a restriction stemming from the chirality of the Hamiltonian in Eq. (1). The

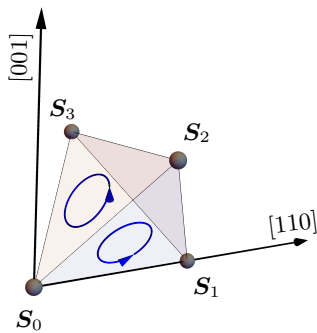


FIG. 1. Illustration of an up-tetrahedron with the direction of the chiral term specified for two of its faces,  $\mathbf{S}_0 \cdot (\mathbf{S}_1 \times \mathbf{S}_2)$  and  $\mathbf{S}_0 \cdot (\mathbf{S}_2 \times \mathbf{S}_3)$ . Here, the black arrow denotes the high-symmetry  $[001]$  and  $[110]$  directions.

identification of the constraints governing the ground-state manifold allow us to study this manifold through an effective 4-state Potts model on the pyrochlore lattice with an additional chiral term. The effective mapping to the 4-state Potts model permits us to identify three intertwined color gauge fields that fulfill an emergent Gauss' law and whose single-tetrahedron fluxes fulfill a right-hand rule in the ground-state manifold. The excitations of this emergent theory are comprised of confined bionic charges with restricted mobility originating from the energetically preferred right-hand rule between the intertwined color gauge fields. The properties of the elementary excitations therefore suggest that this minimal model describes a fractonic system where the ground-state manifold is characterized by at least a sub-extensive degeneracy.

The remainder of the paper is organized as follows: In Sec. II we start by considering the physics of an isolated tetrahedron subject to the chiral interaction. Section III then presents Monte-Carlo results for the full lattice system. In Sec. IV we discuss the low-energy manifold in terms of an effective Potts model and develop a corresponding gauge theory. Section V then presents numerical results for a model which also includes nearest-neighbor Heisenberg interactions. A concluding section closes the paper, while technical details are relegated to the appendices.

## II. SINGLE TETRAHEDRON

As a first approach to the chiral Hamiltonian in Eq. (1) we study the single-tetrahedron case by numerically minimizing the energy of a four-spin configuration through an iterative minimization algorithm [12]. This minimization results in spin configurations where the dot product between two distinct spins equals  $(-1/3)$ . This constraint

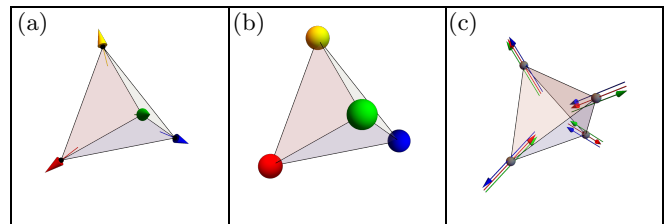


FIG. 2. Example of a single-tetrahedron minimum-energy configuration for the chiral Hamiltonian in Eq. (1) shown in the Heisenberg spin configuration (a), the color representation (b), the Potts gauge fields  $\mathbf{B}_\mu^{(x)}$ ,  $\mathbf{B}_\mu^{(y)}$ , and  $\mathbf{B}_\mu^{(z)}$  colored in red, blue, and green, respectively, in the single tetrahedron (c).

is fulfilled by the spin orientations

$$\mathbf{u}_0 = \frac{1}{\sqrt{3}} (\bar{1}\bar{1}\bar{1}), \quad \mathbf{u}_1 = \frac{1}{\sqrt{3}} (1\bar{1}\bar{1}), \quad (2)$$

$$\mathbf{u}_2 = \frac{1}{\sqrt{3}} (1\bar{1}1), \quad \mathbf{u}_3 = \frac{1}{\sqrt{3}} (\bar{1}11), \quad (3)$$

or equivalently by considering an all-out configuration of the spins as shown in Fig. 2(a) [29]. This constraint permits the construction of alternative ground-state configurations of a single tetrahedron, by applying an *even* permutation of the spin orientations in the single tetrahedron. Note that an odd permutation would instead result in a higher-energy configuration as a consequence of the triple-product term in the Hamiltonian in Eq. (1). To illustrate the construction of the aforementioned single-tetrahedron ground states, up to a global  $O(3)$  rotation, we associate the spin orientations  $\{\mathbf{u}_0, \mathbf{u}_1, \mathbf{u}_2, \mathbf{u}_3\}$  with a unique color,  $\{\text{Red, Blue, Green, Yellow}\} \equiv \{\text{R, B, G, Y}\}$ , which we refer to as the *coloring basis*. This mapping identifies the all-out configuration illustrated in Fig. 2(a) with the colored configuration illustrated in Fig. 2(b). For completeness, we note that there exists yet another representation of the single-tetrahedron configurations in terms of three emergent gauge fields  $\mathbf{B}_\mu^{(c)}$  shown in Fig. 2(c), which we discuss in detail in the subsequent sections. Using the coloring basis, we identify 12 distinct 4-color ground-state configurations obtained by applying even permutations on the all-out configuration [30]; these are shown in Fig. 3.

We note that a spin configuration spanning the entire pyrochlore lattice can be constructed by assigning a spin configuration in Fig. 3 to *all* up tetrahedra while keeping the down tetrahedra in an equivalent low-energy configuration. These configurations possess an energy of  $E_0 = -1.5396J_\chi$  per lattice site.

## III. NUMERICAL ANALYSIS

To investigate the ground states and thermodynamics of the Hamiltonian in Eq. (1) on the full pyrochlore

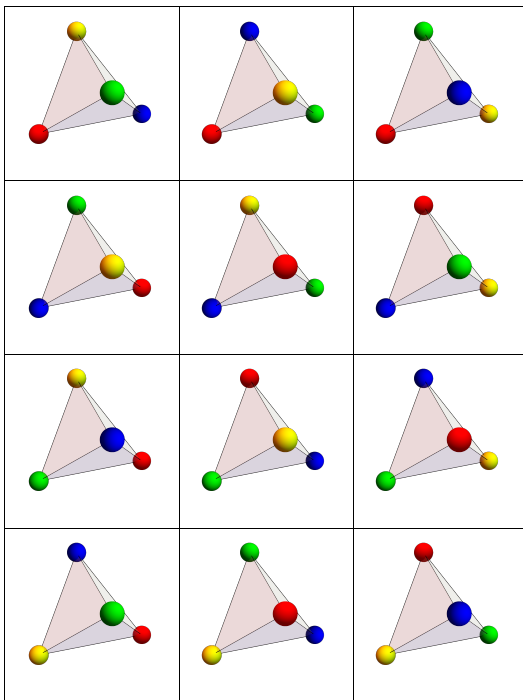


FIG. 3. Single-tetrahedron ground states  $S^x$  of the chiral Hamiltonian in Eq. (1) in the color basis.

lattice, we perform classical Monte-Carlo (cMC) and iterative minimization (IM) simulations considering systems comprised of  $4L^3$  spins with systems of size  $L = 10$ . To thermalize our system, we implement a Gaussian single-spin-flip update [31], an over-relaxation algorithm [32–34], and a multi-valley average between independent cMC simulations inspired by the study of spin glasses [35]. In addition to thermodynamic quantities, we compute the equal-time spin-structure factor.

Figure 4 shows the internal energy and specific heat of the system obtained from a cooling scheme. These quantities smoothly evolve down to low  $T$ , with the specific heat plateauing at a value of  $C/k_B = 1$  and the energy per site tending to  $E \sim -1.52J_\chi$ . No signatures of a transition to a symmetry-broken phase are visible. We note that, although the measured internal energy of the system is very close to the value obtained from the single-tetrahedron analysis, there is a small deviation when this is measured in a cooling-down scheme in cMC. We discuss this deviation, as well as the double-bump structure in  $C(T)$ , in the next section.

To further investigate the finite-temperature behavior of the chiral Hamiltonian in Eq. (1), we study the temperature evolution of the (equal-time) spin-structure factor in three distinct temperature regimes: one for temperatures above the double-bump features, one chosen within the temperature window comprising the double bump, and a temperature well below these features [36] (we refer the reader to Appendix B for the precise expressions of the correlation functions). The resulting structure factor

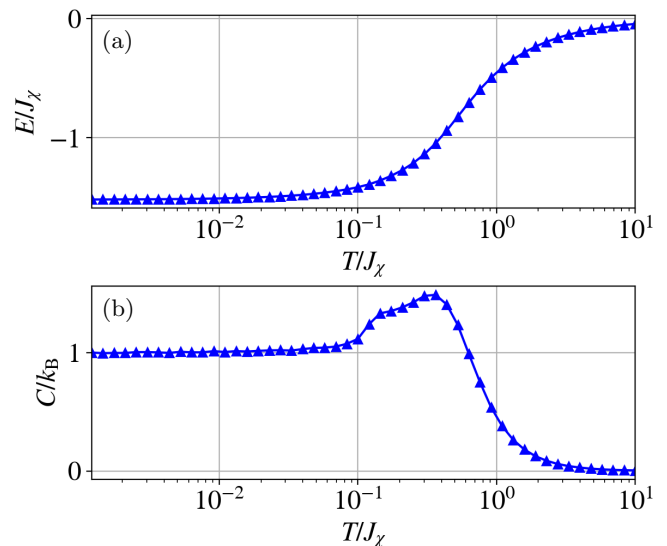


FIG. 4. (a) Internal energy and (b) specific heat per site of the spin chiral Hamiltonian in Eq. (1), showing a smooth evolution as a function of temperature. Note that the specific heat develops a double bump at temperatures of order  $10^{-1}J_\chi$ .

is shown in the  $[hhl]$  and  $[hk0]$  planes in Fig. 5 for the three temperatures considered. At high temperatures, broad features are observed indicating an uncorrelated paramagnetic regime, see Fig. 5(a). As the temperature is decreased these features sharpen up leading to the observation of two-fold pinch points, see Fig. 5(b), indicative of an emergent Gauss' law [4, 9–11, 37–40]. In particular, within the double-bump temperature window features in the diamonds and bow tie patterns appear, in addition to the two-fold pinch points. These additional anisotropic features in the structure factor become more pronounced as the temperature is lowered below the double-bump window resulting in a cross-like pattern in the  $[hk0]$  plane and a dip along the direction of the two-fold pinch points in the  $[hhl]$  plane, see Fig. 5(c).

At high temperatures, the structure-factor profile (the two-fold pinch points and its location) is qualitatively similar to that observed for the pure Heisenberg antiferromagnetic model (HAFM). In the HAFM, the two-fold pinch points are associated with an emergent gauge field abiding by a Gauss' law which in terms of the spin configurations translates into a vanishing magnetization in every tetrahedron [5]. Therefore, the observation of these features in the present model suggests that a similar vanishing magnetization constraint might be present. Indeed, a study of the magnetization distribution reveals that the system realizes a vanishing single-tetrahedron magnetization as the temperatures decreases, see Fig. 6 [41]. This indicates the observation of an energetic antiferromagnetic constraint governing the low-temperature configurations.

The vanishing single-tetrahedron magnetization and the two-fold pinch-point features observed in the spin structure factors suggest that the ground-state manifold

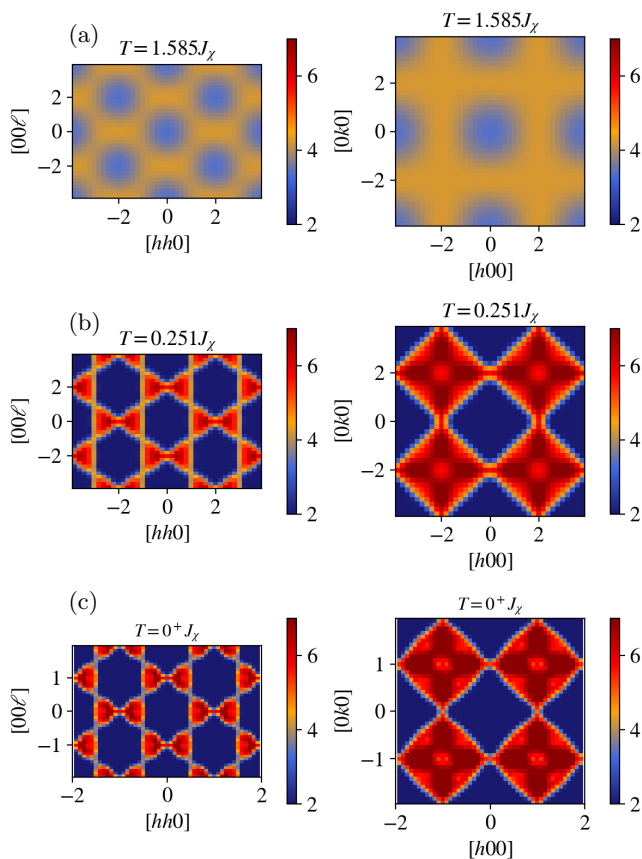


FIG. 5. Equal-time spin structure factor for three distinct temperatures in the high-symmetry  $[hh\ell]$  and  $[hk0]$  scattering planes for the Hamiltonian in Eq. (1) where the formation of sharp two-fold pinch points is observed as the temperature is decreased.

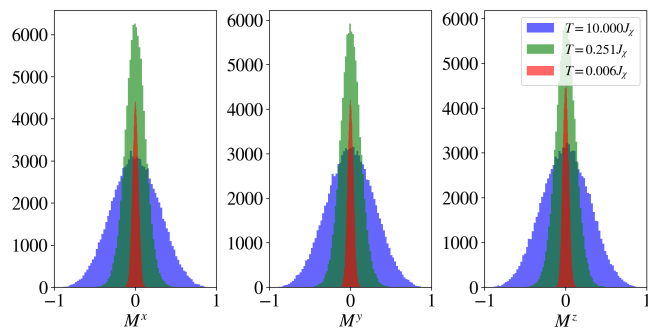


FIG. 6. Histogram of the single-tetrahedron magnetization components for three distinct temperatures of the chiral Hamiltonian in Eq. (1).

of the Hamiltonian in Eq. (1) is conformed by a variety of antiferromagnetic configurations. However, the presence of additional features in the structure factor suggests that further constraints, in addition to the vanishing single-tetrahedron magnetization, exist in the ground-state manifold. This observation is in line with the single-

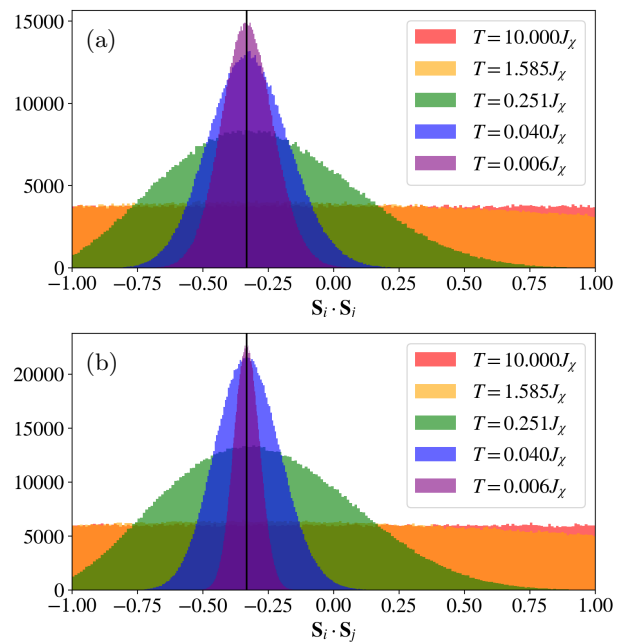


FIG. 7. Histogram of the nearest-neighbor spin correlation,  $\mathbf{S}_i \cdot \mathbf{S}_j$ , for distinct configurations sampled from our cMC simulations for different temperatures obtained for (a) a cool-down and (b) a warm-up scheme. The vertical lines mark the value  $(-1/3)$ , the predicted dot product between neighboring spins in the ground-state manifold.

tetrahedron analysis whose spin configurations, i.e., those shown in Fig. 3, are antiferromagnetic while the spins in a single tetrahedron are constrained to point along the directions  $\{\mathbf{u}_0, \mathbf{u}_1, \mathbf{u}_2, \mathbf{u}_3\}$ , up to a global  $O(3)$  rotation.

To study the onset of this additional constraint as a function of temperature we measure the distribution of the dot product between nearest-neighbor spins. As seen in Fig. 7(a), the distribution develops a peak at the value  $(-1/3)$  for temperatures *below* the double-bump feature in the specific heat, while remaining relatively featureless for higher temperatures. As the temperature is further decreased below the double-bump feature, the distribution becomes sharper while remaining centered at the value of  $(-1/3)$ , suggesting that in the  $T \rightarrow 0$  limit the ground-state configurations are those predicted by the single-tetrahedron analysis. Consequently, we associate the onset of this peak in the distribution with the system entering a temperature regime where the spins in the system progressively adopt a colored configuration.

On passing, we note that for the Hamiltonian in Eq. (1) on the kagome lattice [28] a similar double-bump feature in the specific heat was also observed and associated with the system entering a temperature regime where the spins in a triangle are confined to be pointing along one of the global Cartesian directions [28]. In such a case, however, the low- $T$  specific heat reaches  $C/k_B = 11/12$ , a value associated with quartic spin fluctuations above the ground-state configuration leading to the entropic selection of a symmetry-breaking configuration at low tem-

temperatures over a finite (due to Mermin-Wagner theorem) yet progressively growing correlation radius.

### A. Thermalization and freezing

The lowest energy measured in a cool-down cMC scheme is  $E(T \rightarrow 0^+) \simeq -1.52J_\chi$  (per site), close to the single-tetrahedron ground-state energy of  $E_0 = -1.5396J_\chi$ . However, it is important to note that in a cool-down scheme, our cMC simulations seem to plateau at an energy slightly higher than  $E_0$ . To address the origin of this discrepancy we consider a warm-up scheme starting from an all-out configuration at  $T = 0^+$  and compare the evolution of the dot-product distribution and the internal energy with those obtained from a cool-down scheme, see Fig.7(b) and Fig. 8. As observed for the cool-down scheme, the distribution of the dot product of the warm-up scheme develops a peak centered at  $(-1/3)$  at low temperatures while appearing to be featureless at high temperatures. However, we note that at low temperatures, the distribution of the warm-up scheme appears to be sharper compared to that obtained from a cool-down scheme at the same temperatures [42].

The discrepancy between the cool-down and warm-up evolution procedures can also be observed in the internal energy of the system. Indeed, the energies obtained at low  $T$  within the warm-up scheme are consistent with the single-tetrahedron ground-state energy  $E_0$ , whereas the cool-down scheme levels off at a higher value, see Fig. 8. Although the warm-up scheme better represents the expected internal energy, we note that this procedure appears to be “frozen” in the initial all-out state up to temperatures where the double-bump structure in Fig. 4 is observed. Indeed, the specific heat from the warm-up scheme shows a distinct peak associated with a crossover from a low-temperature ordered phase, the all-out order, to a high-temperature disordered phase. The discrepancy between these two schemes in addition to the freezing of the warm-up scheme suggests that the cool-down scheme finds a locally stable configuration while the warm-up scheme is trapped in the global energy minimum. Indeed, we have verified that this low-temperature freezing is also observed when the starting warm-up state is not a perfect  $\mathbf{k} = \mathbf{0}$  state, suggesting that the freezing at low temperatures is independent of the starting 4-color configuration for reasons we discuss below. For more details on the warm-up scheme, we refer the reader to Appendix E.

The variation of thermodynamic quantities measured depending on the different sampling schemes is characteristic of spin-glass systems [43–45], of certain spin-liquids where non-local updates are needed to *tunnel* between distinct ground-state configurations or to move and annihilate excitations [12, 15], and of fractonic systems [46, 47]. In the next section, we discuss such a scenario by identifying an effective gauge theory describing the ground-state manifold which reveals the emergence of

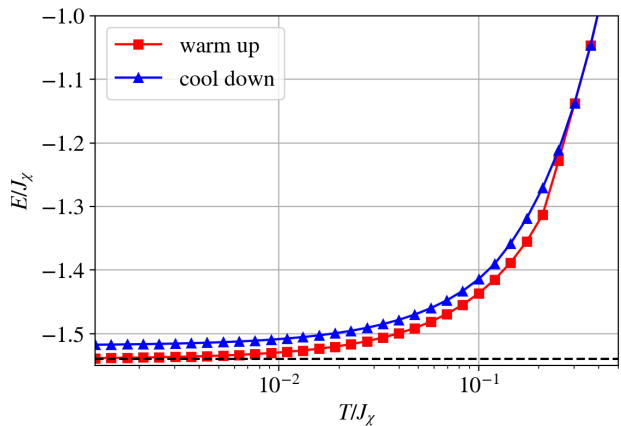


FIG. 8. Internal energy per lattice site obtained using a warm-up and a cool-down scheme in a classical Monte-Carlo simulation. The dashed line indicates the energy  $E_0 = -1.5396J_\chi$  of the single-tetrahedron ground state.

complex gauge charges that are directly correlated with the freezing and responsible for the mismatch between the warm-up and cool-down schemes. For more details on the evolution of the cMC results and the cool-down procedure, we refer the reader to Appendix E.

## IV. EFFECTIVE POTTS MODEL AND GROUND-STATE MANIFOLD

The construction of the ground-state manifold is greatly simplified by considering distinct tiling patterns of 4-color states, however, this construction does not provide us with an effective theory describing the low-temperature physics of this model. Indeed, a common hallmark of classical spin-liquids is the emergence of a low-temperature field theory which associates the constraints of the ground-state manifold with the appearance of a gauge symmetry [48]. Nevertheless, the characterization of the ground-state manifold employing the 4-color mapping suggests that a theory describing the low-temperature spin-liquid phase is associated with a type of antiferromagnetic  $q$ -state Potts Hamiltonian with  $q = 4$  whose ground-state manifold is given by the 4-color states shown in Fig. 3. The regular 4-state Potts model, however, allows *all* 4-color states per tetrahedron. Thus, in order to preserve only the configurations listed in Fig. 3, we consider the modified Potts Hamiltonian

$$\mathcal{H}_\chi^{\text{Potts}} = J \sum_{i,j} \delta_{q_i, q_j} + J_\chi \sum_{\boxtimes} \left( 1 - \delta \left( S^{\boxtimes}, S^\times \right) \right), \quad (4)$$

where the first term corresponds to the usual Potts interaction, and the second term corresponds to an energy cost  $J_\chi$  given a 4-color state  $S^{\boxtimes}$  that is *not* a part of the list of 4-color states  $S^\times$  shown in Fig. 3, i.e., the configurations obtained by performing odd permutations on the all-out 4-color state. We refer to this second term as



a *chiral* term for reasons which will become clear in the subsequent discussion.

By construction, the ground-state configuration of the Hamiltonian in Eq. (4) (with the built-in constraint of having vanishing internal energy) corresponds to ground-state configurations of the chiral Hamiltonian in Eq. (1). Indeed, such equivalence can be numerically established by obtaining ground-state configurations from the Hamiltonian in Eq. (4) via a cMC and then translating these into the corresponding Heisenberg spin configurations to successively compute the energy for the Hamiltonian in Eq. (1). This comparison does show that all 4-color configurations obtained from the Hamiltonian in Eq. (4) translate into ground-state configurations of the chiral Hamiltonian (not shown) [49].

### A. Regular Potts model

Having demonstrated that the two models in Eq. (1) and Eq. (4) result in a similar ground-state manifold, we now construct an effective gauge theory capable of describing the correlations observed in the ground-state manifold of the Potts Hamiltonian and, by extension, the chiral Hamiltonian. As a starting point, we consider the *regular* Potts model, i.e., the one with  $J_\chi = 0$ , whose gauge theory on the pyrochlore lattice for the antiferromagnetic case was studied in Ref. [50]. The regular 4-state Potts model in this lattice can be described by an effective field theory where three intertwined gauge fields  $\{\mathbf{B}_\mu^{(c)}\}$  identified by the index  $c \in \{x, y, z\}$  are defined as

$$\mathbf{B}_\mu^{(c)}(\mathbf{r}) = S_\mu^c(\mathbf{r})\mathbf{z}_\mu, \quad (5)$$

where  $\mu$  labels the sublattice index,  $\mathbf{r}$  denotes a FCC lattice vector,  $c$  also indexes the spin component, and  $\mathbf{z}_\mu$  is the *local*  $z$  direction of the spin in sublattice  $\mu$ , see Appendix A for the definition of the local  $z$  directions. In this basis, the all-out configuration is associated with the gauge field configuration illustrated in Fig. 2(c). In the ground-state manifold, the spin  $\mathbf{S}_\mu(\mathbf{r})$  corresponds to one of the four possible color orientations  $\{\mathbf{R}, \mathbf{B}, \mathbf{G}, \mathbf{Y}\} \equiv \{\mathbf{u}_0, \mathbf{u}_1, \mathbf{u}_2, \mathbf{u}_3\}$ . At low temperatures, the three intertwined fields follow an energetically imposed 2-In-2-Out constraint indicating an emergent Gauss' law  $\nabla \cdot \mathbf{B}^{(c)} = 0$ , see Appendix C for all the ground-state single-tetrahedron gauge field configurations. This construction identifies an effective Hamiltonian for the  $q = 4$  Potts model provided by

$$\mathcal{H}_{\text{eff}}(J_\chi = 0) \propto \int d\mathbf{r} \left[ J \sum_c |\nabla \cdot \mathbf{B}^{(c)}(\mathbf{r})|^2 \right]. \quad (6)$$

This effective low-temperature gauge-field theory in Eq. (6) implies that in the ground-state manifold the gauge fields fulfill a divergence-free condition [4, 51], equivalent to that of spin-ice, indicating that the field lines associated with these fields can have no boundaries and therefore consist of closed loops.

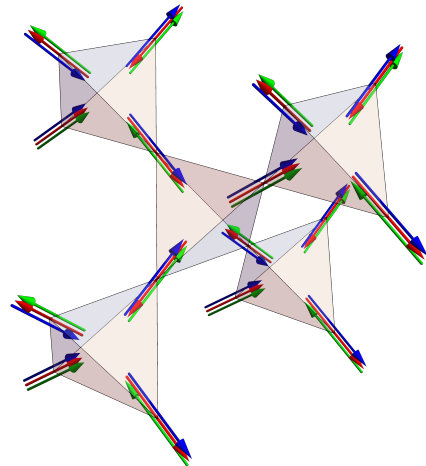


FIG. 9. Configuration of the Potts gauge fields  $\mathbf{B}_\mu^{(c)}$  for a  $q = 0$  ground-state configuration. Here, the red, blue and green arrows denote the local orientations of the  $\mathbf{B}_\mu^{(x)}$ ,  $\mathbf{B}_\mu^{(y)}$ , and  $\mathbf{B}_\mu^{(z)}$  fields, respectively. Note that every tetrahedron obeys a two-in–two-out rule for each Potts field, corresponding to a state with no charges associated to any field.

In Fig. 9, we show a gauge field configuration for a state in the ground-state manifold. Extending the similarities with the spin-ice phase, distinct ground-state configurations of this model can be obtained by identifying closed loops conformed by two colors and then interchanging the colors in the loop. In contrast with spin ice, violations of the divergence-free condition results in the generation of two gauge charges, dubbed *bions*, which violate the divergence-free constraints of *two* gauge fields concurrently and result in an energetic cost proportional to  $J$ . For the regular Potts Hamiltonian, the bions are free to move with no additional energy cost and are connected by “Dirac strings” colored by the gauge fields associated with the bions. In Fig. 10, we illustrate a high-energy gauge configuration resulting from applying an even permutation of the color degrees of freedom to the tetrahedron in the center of Fig. 9. This permutation results in the generation of 8 bionic charges where the divergence-free constraint is broken in the tetrahedra where the light-colored (dark-colored) bions correspond to positively (negatively) charged bions of the corresponding color field.

### B. Chiral Potts model

Let us now consider the full Potts Hamiltonian with  $J_\chi > 0$  in Eq. (4) which restricts the configurations to only those shown in Fig. 3. It is clear that the inclusion of this chiral term does not change the emergent Gauss' law in the  $\mathbf{B}_\mu^c$  fields as the subset of configurations allowed by the chiral term still fulfills the constraint of having a vanishing  $\nabla \cdot \mathbf{B}^{(c)}$ . The introduction of this term however

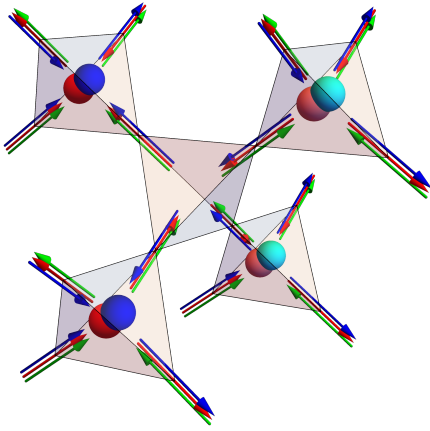


FIG. 10. Configuration of the Potts gauge fields  $\mathbf{B}_\mu^{(c)}$  for a configuration where bionic excitations are present. Here the red, blue and green arrows denote the local orientations of the  $\mathbf{B}_\mu^{(x)}$ ,  $\mathbf{B}_\mu^{(y)}$ , and  $\mathbf{B}_\mu^{(z)}$  fields, respectively. Additionally, the red (blue) spheres represent charges associated with a non-zero Gauss' law of the  $\mathbf{B}_\mu^{(x)}$  ( $\mathbf{B}_\mu^{(y)}$ ) field in the corresponding tetrahedra, where the light (dark) color indicates that the charge is positive (negative).

restricts the allowed *chirality* between the total flux of the three gauge fields in a single tetrahedron defined as

$$\Phi^{(c)}(\mathbf{r}) \equiv \sum_{\mu=0}^3 \mathbf{B}_\mu^{(c)} = \sum_{\mu=0}^3 S_\mu^c(\mathbf{r}) z_\mu, \quad (7)$$

which, in the ground-state manifold, are constrained to be mutually perpendicular, see Appendix D. In other words, the introduction of the chiral term only permits those color configurations for which the product

$$\Phi^{(x)} \cdot (\Phi^{(y)} \times \Phi^{(z)}), \quad (8)$$

yields a positive value. Indeed, listing the allowed single-tetrahedron color configurations (see Fig. 11), illustrates that the chirality of these fields is right-handed.

To make this observation mathematically precise it suffices to associate the even and odd permutations of the permutation group  $\mathcal{S}_4$  with the proper and improper rotations of the tetrahedral group  $T_d$ , respectively. This separation of both the  $\mathcal{S}_4$  and the  $T_d$  groups can be performed by considering the equivalence classes associated by the sign of the permutation and the determinant of the transformation, respectively. The equivalence classes then allow us to identify every even (odd) permutation of the group  $\mathcal{S}_4$  with a proper (improper) rotation in  $T_d$  [52]. By definition, proper rotations do not change the chirality of a mathematical construct, whereas improper rotations do. This property implies that the chirality between the fluxes in the ground-state manifold is a “built-in” energetic restriction of the Hamiltonian considered in Eq. (4). Consequently, and motivated by the effective theory of the regular Potts model, we propose

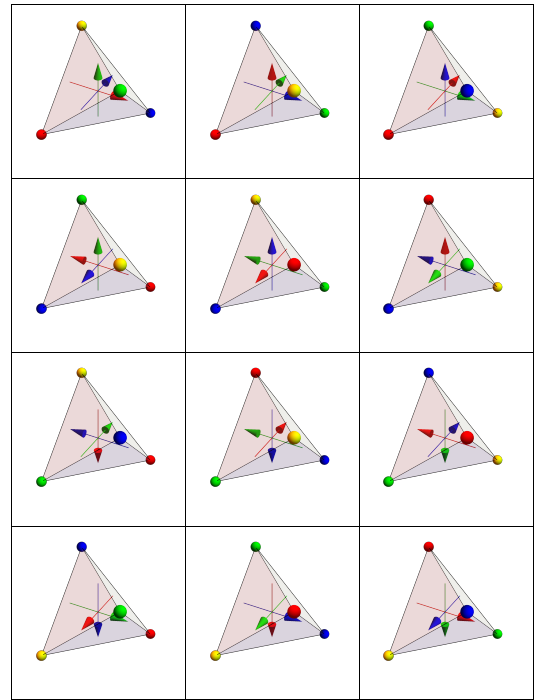


FIG. 11. Single-tetrahedron ground-state configuration in the color basis with the total flux  $\Phi^{(c)}$  corresponding to the gauge fields  $\mathbf{B}_\mu^{(c)}$  shown in the center of each tetrahedron where the red, blue, and green arrows correspond to the  $\Phi^{(x)}$ ,  $\Phi^{(y)}$ , and  $\Phi^{(z)}$  fluxes, respectively.

a minimal phenomenological effective gauge theory that encompasses all the restrictions for the gauge fields

$$\mathcal{H}_{\text{eff}} = \int d\mathbf{r} \left[ J \sum_c |\nabla \cdot \mathbf{B}^{(c)}|^2 - J_\chi \Phi^{(x)} \cdot (\Phi^{(y)} \times \Phi^{(z)}) \right], \quad (9)$$

where the first term constrains the gauge fields to be divergence-free while the second term enforces the right-hand chirality between the fluxes with  $J_\chi$  being defined as a phenomenological positive constant. Note that the proposed theory breaks time-reversal symmetry as it is composed of both two-body and three-body terms. This is natural given that the original Hamiltonian in Eq. (1) breaks time-reversal symmetry as well.

### C. Excitations of the chiral Potts model

The introduction of the chiral term in the Hamiltonian adds an energy cost  $J_\chi$  to the divergence-free gauge field configurations which results in a left-hand chirality of the total fluxes  $\Phi^{(c)}$ . This apparent small modification to the Potts Hamiltonian results in crucial differences in the ground-state manifold of the Potts model and its excitations. Indeed, flipping closed-colored-loops connecting two different ground-state configurations of the *regular* Potts model now results in high-energy configurations of

the *chiral* Potts model whose energy grows proportional to the length of the closed loop: closed loops can be regarded as a chain of odd single-tetrahedra permutations where each permutation has an energy cost of  $J_\chi$ .

Consequently, the Dirac strings connecting the bionic excitations now have a tension, associated with its length, resulting in the confinement of the bionic charges. It is then natural to ask what type of a non-local update connects distinct ground-state configurations which is constructed from even permutations in all the tetrahedra involved. Note, however, that the relation of this update with proper rotations (even permutations) implies that such a non-local transformation *must* be a closed 2-dimensional surface as every tetrahedra involve updates at least three of its four corners. Similar types of transformations have been studied in fractonic systems where the closed surfaces can be associated with the creation and posterior annihilation of fractonic charges [46].

Indeed, starting from a  $\mathbf{k} = \mathbf{0}$  state, the simplest non-local transformation is identified as one that produces an even permutation in all the triangles of an aleatory selected kagome plane. Through this sole transformation we can identify a minimum degeneracy in the ground-state manifold which scales with the linear size  $L$ , and not with the number of sites  $L^3$ , indicating that the ground-state manifold has at least a sub-extensive degeneracy associated with these transformations. These higher-dimensional non-local updates can be associated with the *restricted* motion of the bionic charges, suggesting that the bionic charges of the regular Potts model are *fracton* charges in the chiral Potts model. We leave the study of these charges and a more detailed characterization of the model in Eq. (4) for future work.

## V. CHIRAL AND HEISENBERG INTERACTIONS

As previously mentioned, the chiral Hamiltonian in Eq. (1) is one of the lower-order corrections when considering a Hubbard model with an applied magnetic field. This chiral term, however, is obtained as the next-to-leading order interaction *after* the usual Heisenberg interaction. It is therefore natural to inquire about the behavior of the Hamiltonian

$$\mathcal{H} = J \sum_{\langle ij \rangle} \mathbf{S}_i \cdot \mathbf{S}_j - J_\chi \sum_{i,j,k \in \Delta} \chi_{ijk}, \quad (10)$$

which now includes both the chiral and the Heisenberg term  $J$  with  $J > 0$ . Naïvely, one could expect that the introduction of the Heisenberg interaction radically changes the overall physical behavior of the system depending on the ratio of the interactions  $J/J_\chi$ . However, as was mentioned in Sec. III, the ground-state manifold resulting from the chiral interaction obeys a vanishing magnetization constraint which is the sole constraint imposed by the Heisenberg interaction. Consequently, the ground-state manifold of the Hamiltonian in Eq. (10)

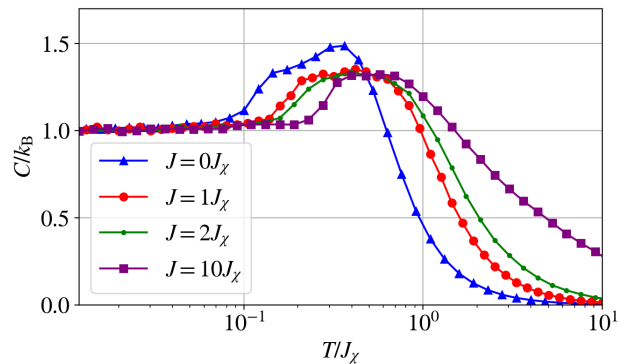


FIG. 12. Specific heat of the Hamiltonian in Eq. (10) for various values of the Heisenberg coupling  $J$ . Here the double-bump feature is only seen for the case  $J = 0$  and  $J = J_\chi$ , whereas a single bump is observed for higher values of  $J$ .

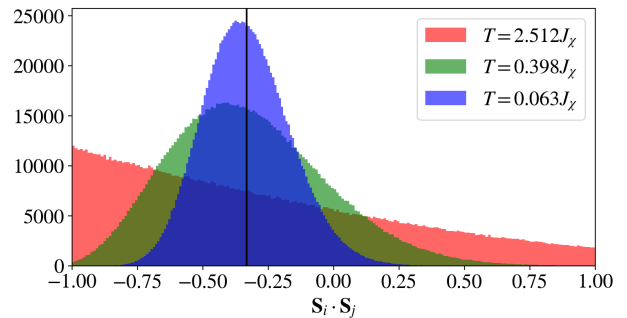


FIG. 13. Histogram of nearest-neighbor spin correlations for three different temperatures measured for the Hamiltonian in Eq. (10) with  $J = 10J_\chi$ .

matches that of the Hamiltonian in Eq. (1). However, this does not imply that the thermodynamics of these systems is equivalent. Indeed, the introduction of a Heisenberg interaction modifies the behavior of the specific heat whereby the double-bump structure observed for the chiral Hamiltonian (1) is no longer present for a sufficiently large value of  $J$  and is instead replaced by a single broad bump, see Fig. 12.

The location in temperature of this single bump appears to be relatively stable to the value of  $J$ , suggesting a relation of this feature with the chiral interaction parameter  $J_\chi$  and the onset of the chiral constraints on the ground state. Indeed, similar to the case for pure chiral Hamiltonian for which  $J = 0$ , by studying the distribution of the dot product between neighboring spins, we find that this distribution develops a peak close to the value of  $(-1/3)$  when this bump is reached and keeps on sharpening and approaching this value as the temperature is further decreased, see Fig. 13 for the case of  $J = 10J_\chi$ . It is worth mentioning that the shape of this distribution in the antiferromagnetic Heisenberg Hamiltonian with no chiral interaction, i.e.,  $J_\chi = 0$  and  $J = 1$ , resembles the shape of the high-temperature distribution in Fig. 13 down to the lowest temperature, see



Appendix F for further details in the evolution of this distribution.

## VI. CONCLUSION

We have studied the classical limit of the chiral Hamiltonian in Eq. (1) on the pyrochlore lattice using numerical and analytical tools to describe its thermodynamics and characterize the Hamiltonian’s ground-state manifold. Our results suggest that the chiral Hamiltonian realizes a classical spin-liquid phase at low temperatures where the excitations behave as fractons, i.e., quasiparticles with restricted mobility [38, 39, 46, 53]. We model the ground-state manifold of this novel spin-liquid by identifying 4 distinct orientations where the spins in a single tetrahedron are constrained to point along (up to global  $U(1)$  rotations) in the  $T \rightarrow 0$  limit. This constraint allows us to characterize the ground-state manifold in terms of a 4-state Potts model [50] and identify an emergent gauge theory. The effective theory employs three rank-1 fields which, in the ground-state manifold, become divergence-free and whose intertwined fluxes in a single tetrahedron follow a right-hand rule. The constraints found in the ground-state manifold lead to a sub-extensive degeneracy which can be directly associated with even permutations of the spin states in all the triangles of an infinite kagome plane bisecting the system in two.

The emergent gauge theory identifies the elementary excitations of the system as so-called bions, previously identified as the deconfined elementary excitation of a regular 4-state Potts model [50], which in the chiral model acquire a restricted motion associated with the right-hand rule imposed in the total fluxes through a single tetrahedron. To further investigate the thermodynamics of its elementary excitations and its restricted motion, a non-local numerical algorithm tailored to this system must be developed [54]. The elementary excitations, the sub-extensive degeneracy, and the classical Monte-Carlo simulations presented are all consistent with the typical behavior observed in fracton systems. This therefore identifies the chiral Hamiltonian in Eq. (1) on the pyrochlore lattice as a “simple” fracton model whose further study may shed light on the intricate physics associated with these systems. Finally, we also considered the extension of the chiral model by an additional antiferromagnetic Heisenberg coupling. We demonstrated that the overall properties of the model remain largely unchanged for all strengths of the Heisenberg antiferromagnetic couplings considered.

A natural extension of this work would be to consider a model with a staggered pattern of chirality on up- and down-tetrahedra, similar to what has been studied on the kagome lattice [28]. Moreover, in the context of material realizations, it would be worthwhile to assess the fate of the spin-liquid phase upon adding anisotropic couplings. Last not least, studying the quantum counterpart of the

present chiral model could yield a yet unexplored chiral fractonic quantum spin-liquid.

## ACKNOWLEDGMENTS

We thank Kai Chung, Pedro Consoli, and Han Yan for helpful discussions. D.L.-G. and MV acknowledge financial support from the DFG through the Würzburg-Dresden Cluster of Excellence on Complexity and Topology in Quantum Matter – *ct.qmat* (EXC 2147, project-id 390858490) and through SFB 1143 (project-id 247310070). D.L.-G. is supported by the Hallwachs-Röntgen Postdoc Program of *ct.qmat*. The work of Y.I. was performed in part at the Aspen Center for Physics, which is supported by National Science Foundation Grant No. PHY-2210452. The participation of Y.I. at the Aspen Center for Physics was supported by the Simons Foundation. The research of Y.I. was carried out, in part, at the Kavli Institute for Theoretical Physics in Santa Barbara during the “A New Spin on Quantum Magnets” program in summer 2023, supported by the National Science Foundation under Grant No. NSF PHY-1748958. Y.I. acknowledges support from the ICTP through the Associates Programme and from the Simons Foundation through Grant No. 284558FY19, IIT Madras through the Institute of Eminence (IoE) program for establishing QuCenDiEM (Project No. SP22231244CPETWOQCDHOC), and the International Centre for Theoretical Sciences (ICTS), Bengaluru, India during a visit for participating in the program “Frustrated Metals and Insulators” (Code No. ICTS/frumi2022/9). Y.I. also acknowledges the use of the computing resources at HPCE, IIT Madras.

### Appendix A: Local $z$ directions

In this appendix, we provide the local  $z$  direction of the spins in an up tetrahedron used in the definition of the emergent gauge fields  $\mathbf{B}_\mu^{(c)}$ . The local  $z$  directions  $\mathbf{z}_\mu$  are given by the vectors

$$\mathbf{z}_0 = \frac{1}{\sqrt{3}} (111), \quad \mathbf{z}_1 = \frac{1}{\sqrt{3}} (\bar{1}\bar{1}1), \quad (\text{A1})$$

$$\mathbf{z}_2 = \frac{1}{\sqrt{3}} (\bar{1}1\bar{1}), \quad \mathbf{z}_3 = \frac{1}{\sqrt{3}} (1\bar{1}\bar{1}), \quad (\text{A2})$$

where  $\mu$  labels the sublattice basis as shown in Fig. 1.

### Appendix B: Spin structure factor

In this appendix, we provide the expressions for the spin-spin correlation functions used in the main text. For the pyrochlore lattice, a non-Bravais lattice with a sublattice basis of 4, the most general correlation between

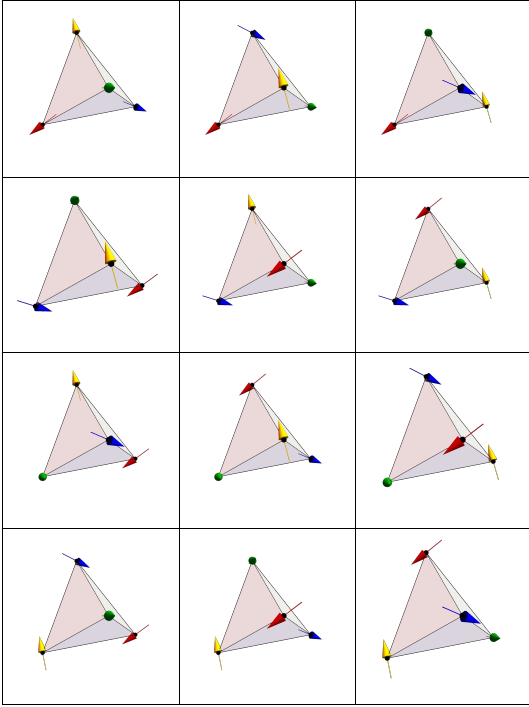


FIG. 14. Single-tetrahedron spin  $\mathbf{S}_\mu$  configuration where the spins in each tetrahedron are oriented along one of the  $\{\mathbf{u}_0, \mathbf{u}_1, \mathbf{u}_2, \mathbf{u}_3\}$  orientations and colored according to the transformation  $\{\mathbf{u}_0, \mathbf{u}_1, \mathbf{u}_2, \mathbf{u}_3\} \equiv \{R, B, G, Y\}$ .

the  $\alpha$  and  $\beta$  components of the spins in sublattice  $\mu$  and  $\nu$  is given by

$$S_{\mu\nu}^{\alpha\gamma}(\mathbf{k}) = \langle S_\mu^\alpha(\mathbf{k}) S_\nu^\gamma(-\mathbf{k}) \rangle. \quad (\text{B1})$$

Using this generic correlation function, the spin-spin correlation function is obtained by summing over the trace of spin components

$$\begin{aligned} \mathcal{S}(\mathbf{k}) &= \sum_{\alpha,\beta} \sum_{\mu,\nu} \delta_{\alpha\beta} S_{\mu\nu}^{\alpha\beta}(\mathbf{k}) \\ &= \sum_{\alpha,\beta} \sum_{\mu,\nu} \delta_{\alpha\beta} \langle S_\mu^\alpha(\mathbf{k}) S_\nu^\beta(-\mathbf{k}) \rangle. \end{aligned} \quad (\text{B2})$$

For completeness, we provide the experimentally measurable unpolarized neutron structure factor,

$$\mathcal{S}_\perp(\mathbf{k}) = \sum_{\alpha,\beta} \sum_{\mu,\nu} \left( \delta_{\alpha\beta} - \hat{k}^\alpha \hat{k}^\beta \right) \langle S_\mu^\alpha(\mathbf{k}) S_\nu^\beta(-\mathbf{k}) \rangle \quad (\text{B3})$$

It is worth noting that, since the chiral Hamiltonian in Eq. (1) preserves a global  $O(3)$  symmetry in the spin degrees of freedom, the unpolarized neutron structure factor for this system presents the same features as those illustrated in the spin-spin correlation function with a diminished intensity originating from the neutron projection.

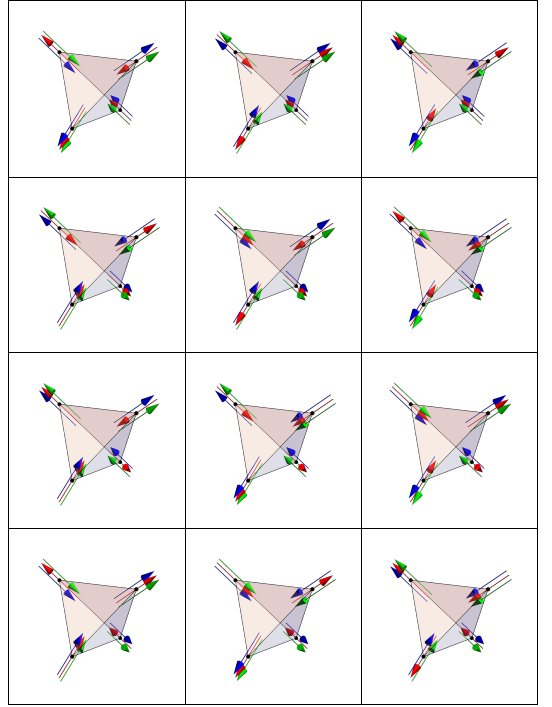


FIG. 15. Single-tetrahedron gauge-field  $\mathbf{B}_\mu^{(c)}$  configuration where the red, blue, and green colors correspond to the  $\mathbf{B}_\mu^{(x)}$ ,  $\mathbf{B}_\mu^{(y)}$  and  $\mathbf{B}_\mu^{(z)}$  fields, respectively.

### Appendix C: Single-tetrahedron spin and gauge-field configurations

In this appendix, we provide the 12 single-tetrahedron spin  $\mathbf{S}_\mu$  and gauge-field  $\mathbf{B}_\mu^{(c)}$  configurations, see Fig. 14 and Fig. 15, respectively. As discussed in the main text, we assign a color to the orientations  $\{\mathbf{u}_0, \mathbf{u}_1, \mathbf{u}_2, \mathbf{u}_3\} \equiv \{R, B, G, Y\}$  which can be seen in Fig. 14 accordingly.

### Appendix D: Color gauge fields and orthogonality of the fluxes

In this appendix, we provide further information regarding the three color gauge fields  $\mathbf{B}_\mu^{(c)}$  and the associated total flux  $\Phi^{(c)} \equiv \sum_\mu \mathbf{B}_\mu^{(c)}$  defined in the main text and illustrated in Fig. 16. As was previously pointed out in the main text, in the absence of gauge charges, the three color fluxes in every single tetrahedron are constrained to be perpendicular. Indeed, from the definition of the color fields one obtains

$$\begin{aligned} \Phi^b \cdot \Phi^c &= \sum_\mu S_\mu^b z_\mu \sum_\nu S_\nu^c z_\nu \\ &= \sum_\mu S_\mu^b S_\mu^c - \frac{1}{3} \sum_{\mu \neq \nu} S_\mu^b S_\nu^c \\ &= \frac{16}{9} \delta_{b,c}, \end{aligned} \quad (\text{D1})$$

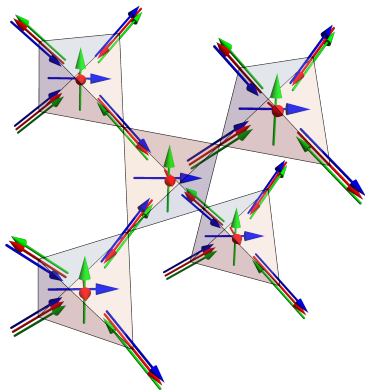


FIG. 16. Color gauge fields  $\mathbf{B}_\mu^{(c)}$  defined on the pyrochlore lattice sites and the corresponding gauge flux  $\Phi^{(c)}$  through each tetrahedron shown in the center of the corresponding tetrahedra for a simple  $\mathbf{k} = 0$  configuration.

where we have used the fact that in the ground-state manifold  $\sum_\mu S_\mu^c = 0$ , and that distinct single-tetrahedron coloring configurations are orthogonal to each other.

### Appendix E: Thermodynamics from warm-up and cool-down schemes

In this appendix, we present the specific heat and energy evolution obtained through warm-up and cool-down cMC schemes used to study the chiral Hamiltonian in Eq. (1). In Fig. 17, we show results for two initial configurations employed in the warm-up scheme, namely, (i) a  $\mathbf{k} = 0$  configuration and (ii) a configuration obtained from a  $\mathbf{k} = 0$  configuration by applying a non-local energy-conserving transformation on an infinite kagome plane. We henceforth refer to these initial states as the  $\mathbf{k} = 0$  state and the kagome state, respectively. For the warm-up schemes, the energy and specific heat of both the  $\mathbf{k} = 0$  and the kagome configurations result in a similar behavior where the internal energy plateaus to the predicted value of  $E_0$ , and a peak in the specific heat is observed. As previously discussed in the main text, the  $\mathbf{k} = 0$  warm-up scheme presents a peak in the specific heat associated with the onset of the all-out order from which the warm-up system was initialized. The observation of this peak in the specific heat of the warm-up scheme is associated with the crossover from the starting  $\mathbf{k} = 0$  chiral order to a disorder paramagnet. A similar behavior is observed for the warm-up scheme obtained from the initial kagome state where the peak is then associated to the onset of a *partially* ordered configuration. Indeed, if we measure the mean sublattice magnetization [55]

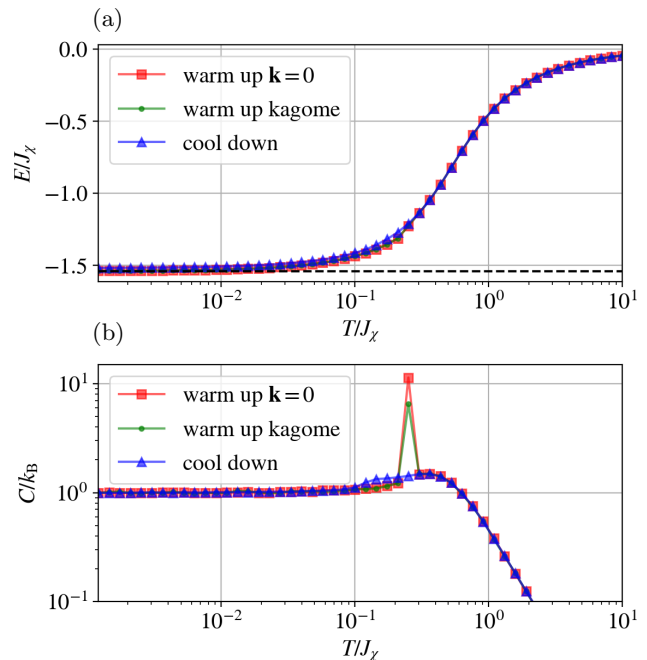


FIG. 17. (a) Internal energy and (b) specific heat per lattice site obtained using a warm-up and a cool-down scheme in a classical Monte-Carlo simulation. As in Fig.7, the dashed line indicates the energy  $E_0 = -1.5396J_\chi$  predicted for a single-tetrahedron ground state.

$$m_s^2 = \frac{4}{N^2} \left\langle \sum_\mu \left| \sum_{\mathbf{r}} \mathbf{S}_\mu(\mathbf{r}) \right|^2 \right\rangle \quad (\text{E1})$$

where  $\mathbf{r}$  labels the FCC positions,  $\mu$  the sublattice index, and  $N$  corresponds to the number of spins in the system, we observe how this parameter saturates at one for the  $\mathbf{k} = 0$  warm-up scheme and to an intermediate value for the kagome warm-up scheme, while it vanishes for the cool-down scheme, see Fig. 18. In contrast, the observation of two bumps in the cool-down scheme is associated with two crossovers; one entering the antiferromagnetic manifold and a second one signaling the crossover to the chiral phase. We refrain from further commenting on these features as we believe that the warm-up scheme presents freezing in the low-temperature configuration due to the lack of a non-local update in the cMC implementation as mentioned in the main text.

### Appendix F: Evolution of the nearest-neighbor spin correlations in the Heisenberg antiferromagnet

In this appendix, we provide the evolution of the distribution of the dot product between nearest-neighbor spins for the pure Heisenberg antiferromagnetic model, see Fig. 19. Although this distribution is not centered at  $(-1/3)$ , its average value is  $(-1/3)$  which coincides with the average value one would obtain for the distribution

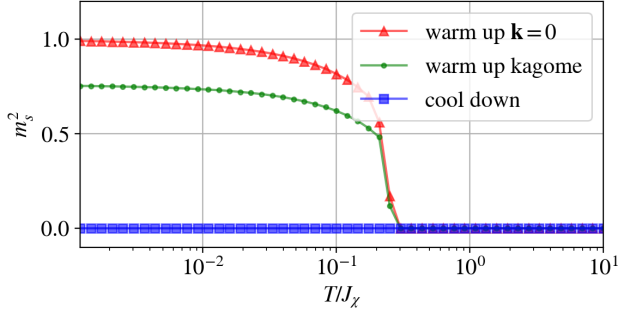


FIG. 18. Mean sublattice magnetization  $m_s^2$  obtained using a warm-up and a cool-down scheme in a classical Monte-Carlo simulation.

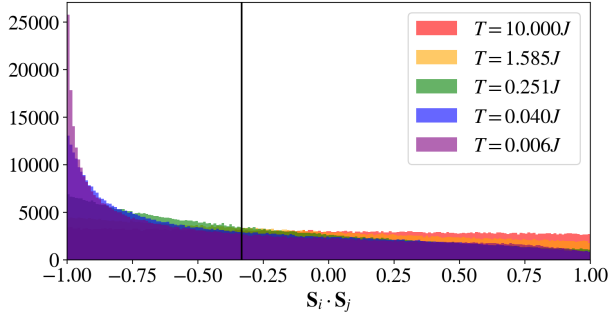


FIG. 19. Histogram of the nearest-neighbor spin correlations for different temperatures obtained for a cool-down scheme for the bare Heisenberg antiferromagnetic Hamiltonian.

in the chiral manifold. In fact, this equal average value motivated us to study the full distributions of the dot product instead of only its average to detect the onset of the chiral constraint as a function of temperature.

- 
- [1] L. Balents, Spin liquids in frustrated magnets, *Nature (London)* **464**, 199 (2010).
- [2] L. Savary and L. Balents, Quantum spin liquids: A review, *Rep. Prog. Phys.* **80**, 016502 (2016).
- [3] C. Castelnovo, R. Moessner, and S. L. Sondhi, Magnetic monopoles in spin ice, *Nature (London)* **451**, 42 (2008).
- [4] C. Castelnovo, R. Moessner, and S. L. Sondhi, Spin Ice, Fractionalization, and Topological Order, *Annu. Rev. Condens. Matter Phys.* **3**, 35 (2012).
- [5] R. Moessner and J. T. Chalker, Properties of a Classical Spin Liquid: The Heisenberg Pyrochlore Antiferromagnet, *Phys. Rev. Lett.* **80**, 2929 (1998).
- [6] S. T. Bramwell and M. J. P. Gingras, Spin ice state in frustrated magnetic pyrochlore materials, *Science* **294**, 1495 (2001).
- [7] O. Benton, L. D. C. Jaubert, H. Yan, and N. Shannon, A spin-liquid with pinch-line singularities on the pyrochlore lattice, *Nat. Commun.* **7**, 11572 (2016).
- [8] H. Yan, O. Benton, L. D. C. Jaubert, and N. Shannon, Rank-2 U(1) Spin Liquid on the Breathing Pyrochlore Lattice, *Phys. Rev. Lett.* **124**, 127203 (2020).
- [9] O. Benton and R. Moessner, Topological route to new and unusual coulomb spin liquids, *Phys. Rev. Lett.* **127**, 107202 (2021).
- [10] H. Yan, O. Benton, A. H. Nevidomskyy, and R. Moessner, Classification of classical spin liquids: Detailed formalism and suite of examples (2023), [arXiv:2305.19189](https://arxiv.org/abs/2305.19189) [[cond-mat.str-el](https://arxiv.org/abs/2305.19189)].
- [11] H. Yan, O. Benton, R. Moessner, and A. H. Nevidomskyy, Classification of classical spin liquids: Typology and resulting landscape (2023), [arXiv:2305.00155](https://arxiv.org/abs/2305.00155) [[cond-mat.str-el](https://arxiv.org/abs/2305.00155)].
- [12] D. Lozano-Gómez, V. Noculak, J. Oitmaa, R. R. P. Singh, Y. Iqbal, J. Reuther, and M. J. P. Gingras, Competing Gauge Fields and Entropically-Driven Spin Liquid to Spin Liquid Transition in non-Kramers Pyrochlores (2023), [arXiv:2310.16682](https://arxiv.org/abs/2310.16682) [[cond-mat.str-el](https://arxiv.org/abs/2310.16682)].
- [13] M. J. P. Gingras and P. A. McClarty, Quantum spin ice: a search for gapless quantum spin liquids in pyrochlore magnets, *Rep. Prog. Phys.* **77**, 056501 (2014).
- [14] N. Niggemann, Y. Iqbal, and J. Reuther, Quantum Effects on Unconventional Pinch Point Singularities, *Phys. Rev. Lett.* **130**, 196601 (2023).
- [15] K. T. K. Chung and M. J. P. Gingras, 2-Form U(1) Spin Liquids: Classical Model and Quantum Aspects (2023), [arXiv:2310.17607](https://arxiv.org/abs/2310.17607) [[cond-mat.str-el](https://arxiv.org/abs/2310.17607)].
- [16] M. Taillefumier, O. Benton, H. Yan, L. D. C. Jaubert, and N. Shannon, Competing Spin Liquids and Hidden Spin-Nematic Order in Spin Ice with Frustrated Transverse Exchange, *Phys. Rev. X* **7**, 041057 (2017).
- [17] Y. Iqbal, T. Müller, P. Ghosh, M. J. P. Gingras, H. O. Jeschke, S. Rachel, J. Reuther, and R. Thomale, Quantum and Classical Phases of the Pyrochlore Heisenberg Model with Competing Interactions, *Phys. Rev. X* **9**,

- 011005 (2019).
- [18] V. Noculak, D. Lozano-Gómez, J. Oitmaa, R. R. P. Singh, Y. Iqbal, M. J. P. Gingras, and J. Reuther, Classical and quantum phases of the pyrochlore  $S = \frac{1}{2}$  magnet with Heisenberg and Dzyaloshinskii-Moriya interactions, *Phys. Rev. B* **107**, 214414 (2023).
- [19] S. E. Palmer and J. T. Chalker, Order induced by dipolar interactions in a geometrically frustrated antiferromagnet, *Phys. Rev. B* **62**, 488 (2000).
- [20] J. G. Rau and M. J. P. Gingras, Frustrated quantum rare-earth pyrochlores, *Annu. Rev. Condens. Matter Phys.* **10**, 357 (2019).
- [21] A. M. Hallas, J. Gaudet, and B. D. Gaulin, Experimental insights into ground-state selection of quantum xy pyrochlores, *Annu. Rev. Condens. Matter Phys.* **9**, 105 (2018).
- [22] J. S. Gardner, M. J. P. Gingras, and J. E. Greedan, Magnetic pyrochlore oxides, *Rev. Mod. Phys.* **82**, 53 (2010).
- [23] Y. Wan and M. J. P. Gingras, Color ice states, weathervane modes, and order by disorder in the bilinear-biquadratic pyrochlore heisenberg antiferromagnet, *Phys. Rev. B* **94**, 174417 (2016).
- [24] A. Szabó and G. J. Nilsen, Dynamics of the antiferromagnetic spin ice phase in pyrochlore spinels (2023), [arXiv:2305.16386](https://arxiv.org/abs/2305.16386) [cond-mat.str-el].
- [25] O. I. Motrunich, Orbital magnetic field effects in spin liquid with spinon Fermi sea: Possible application to  $\kappa$ -(ET)<sub>2</sub>Cu<sub>2</sub>(CN)<sub>3</sub>, *Phys. Rev. B* **73**, 155115 (2006).
- [26] X. G. Wen, F. Wilczek, and A. Zee, Chiral spin states and superconductivity, *Phys. Rev. B* **39**, 11413 (1989).
- [27] G. Baskaran, Novel local symmetries and chiral-symmetry-broken phases in  $S=(1/2)$  triangular-lattice Heisenberg model, *Phys. Rev. Lett.* **63**, 2524 (1989).
- [28] J. Pitts, F. L. Buessen, R. Moessner, S. Trebst, and K. Shtengel, Order by disorder in classical kagome antiferromagnets with chiral interactions, *Phys. Rev. Res.* **4**, 043019 (2022).
- [29] We note that the all-in spin configuration, i.e. where all spins point towards the center of the tetrahedron, does *not* correspond to a minimum single-tetrahedron configuration due to the three-body chiral term in the Hamiltonian in Eq. (1), which does not preserve time-reversal symmetry.
- [30] We note that this is simply the dimension of the even permutations in the permutation group  $S_4$ .
- [31] J. D. Alzate-Cardona, D. Sabogal-Suárez, R. F. L. Evans, and E. Restrepo-Parra, Optimal phase space sampling for Monte Carlo simulations of Heisenberg spin systems, *J. Phys. Condens. Matter* **31**, 095802 (2019).
- [32] M. Creutz, Overrelaxation and Monte Carlo simulation, *Phys. Rev. D* **36**, 515 (1987).
- [33] M. E. Zhitomirsky, M. V. Gvozdikova, P. C. W. Holdsworth, and R. Moessner, Quantum Order by Disorder and Accidental Soft Mode in Er<sub>2</sub>Ti<sub>2</sub>O<sub>7</sub>, *Phys. Rev. Lett.* **109**, 077204 (2012).
- [34] M. E. Zhitomirsky, P. C. W. Holdsworth, and R. Moessner, Nature of finite-temperature transition in anisotropic pyrochlore Er<sub>2</sub>Ti<sub>2</sub>O<sub>7</sub>, *Phys. Rev. B* **89**, 140403 (2014).
- [35] P. Chandra, P. Coleman, and I. Ritchey, The anisotropic kagomé antiferromagnet: a topological spin glass?, *J. Phys. I France* **3**, 591 (1993).
- [36] For this last temperature regime we used both cMC and IM to increase the statistics of the measurement.
- [37] S. V. Isakov, K. Gregor, R. Moessner, and S. L. Sondhi, Dipolar Spin Correlations in Classical Pyrochlore Magnets, *Phys. Rev. Lett.* **93**, 167204 (2004).
- [38] M. Pretko, The fracton gauge principle, *Phys. Rev. B* **98**, 115134 (2018).
- [39] M. Pretko, Subdimensional particle structure of higher rank  $U(1)$  spin liquids, *Phys. Rev. B* **95**, 115139 (2017).
- [40] N. Davier, F. A. Gómez Albarracín, H. D. Rosales, and P. Pujol, Combined approach to analyze and classify families of classical spin liquids, *Phys. Rev. B* **108**, 054408 (2023).
- [41] This observation should, however, come as no surprise since a collinear configuration of spins in a single-tetrahedron result in a high-energy configuration. This can be seen by simple inspection of the Hamiltonian in Eq. (1) as a collinear configuration results in a vanishing energy per tetrahedra.
- [42] We have checked that for lower temperatures than the ones reported in Fig. 7, the distribution of the warm-up scheme sharpens towards a Delta distribution centered at  $(-1/3)$ .
- [43] S. F. Edwards and P. W. Anderson, Theory of spin glasses, *J. Phys. F: Met. Phys.* **5**, 965 (1975).
- [44] E. Vincent, Spin glass experiments, in *Encyclopedia of Condensed Matter Physics (Second Edition)*, edited by T. Chakraborty (Academic Press, Oxford, 2024) second edition ed., pp. 371–387.
- [45] K. H. Fischer and J. A. Hertz, *Spin Glasses*, Cambridge Studies in Magnetism (Cambridge University Press, 1991).
- [46] R. M. Nandkishore and M. Hermele, Fractons, *Annu. Rev. Condens. Matter Phys.* **10**, 295 (2019).
- [47] A. Gromov and L. Radzihovsky, Colloquium: Fracton matter, *Rev. Mod. Phys.* **96**, 011001 (2024).
- [48] J. Knolle and R. Moessner, A field guide to spin liquids, *Annu. Rev. Condens. Matter Phys.* **10**, 451 (2019).
- [49] This equivalence can also be tested analytically, as the energy of all configurations in Fig. 3 is replicated in all tetrahedra assuming a perfect tiling can be performed in the full lattice.
- [50] V. Khemani, R. Moessner, S. A. Parameswaran, and S. L. Sondhi, Bionic coulomb phase on the pyrochlore lattice, *Phys. Rev. B* **86**, 054411 (2012).
- [51] K. T. K. Chung, J. S. K. Goh, A. Mukherjee, W. Jin, D. Lozano-Gómez, and M. J. P. Gingras, Probing Flat Band Physics in Spin Ice Systems via Polarized Neutron Scattering, *Phys. Rev. Lett.* **128**, 107201 (2022).
- [52] Indeed note that the single-tetrahedron configurations shown in Fig. 11 can be obtained from *proper* rotations of the single-tetrahedron group  $T_d$  starting from the all-out configuration in Fig. 2(b).
- [53] R. Flores-Calderón, O. Benton, and R. Moessner, Irrational moments and signatures of higher-rank gauge theories in diluted classical spin liquids (2024), [arXiv:2402.03083](https://arxiv.org/abs/2402.03083) [cond-mat.str-el].
- [54] B. Placke, O. Benton, and R. Moessner, Ising fracton spin liquid on the honeycomb lattice (2023), [arXiv:2306.13151](https://arxiv.org/abs/2306.13151) [cond-mat.str-el].
- [55] J. N. Reimers, Absence of long-range order in a three-dimensional geometrically frustrated antiferromagnet, *Phys. Rev. B* **45**, 7287 (1992).